Research Article | Vol. 27, No. 3 | 4 Feb 2019 | OPTICS EXPRESS 1798

Optics EXPRESS

Resonant-antiresonant coupled cavity VCSELs

KEVIN T. COOK,[1] PENGFEI QIAO,[1] JIPENG QI,[1] LARRY A. COLDREN,[2] AND CONNIE J. CHANG-HASNAIN[1,*]

[1] *Department of Electrical Engineering and Computer Sciences and Tsinghua-Berkeley Shenzhen Institute, University of California at Berkeley, Berkeley, CA 94720, USA*
[2] *Departments of Electrical and Computer Engineering and Materials, University of California at Santa Barbara, Santa Barbara, CA 93106, USA*
**cch@berkeley.edu*

Abstract: The wavelength tuning range of a tunable vertical-cavity surface-emitting laser (VCSEL) is strongly influenced by the design of the interface between the semiconductor cavity and the air cavity. A simplified model is used to investigate the origin of the dramatic differences in free spectral range (FSR) and tuning slope observed in semiconductor cavity dominant, extended cavity, and air cavity dominant VCSELs. The differences arise from the positioning of the resonant and antiresonant wavelengths of the semiconductor cavity with respect to the center wavelength. The air cavity dominant design is realized by designing an antiresonant semiconductor cavity, resulting in a larger tuning slope near the center of the tuning range and a wider FSR toward the edges of the tuning range. The findings from the simplified model are confirmed with the simulation of a full VCSEL structure. Using an air cavity dominant design, an electrically pumped laser with a tuning range of 68.38 nm centered at 1056.7 nm at a 550 kHz sweep rate is demonstrated with continuous wave emission at room temperature. This epitaxial design rule can be used to increase the tuning range of tunable VCSELs, making them more applicable in swept-source optical coherence tomography and frequency-modulated continuous-wave LIDAR systems.

1. Introduction

Wavelength-swept lasers are important components in modern optical communications, light detection and ranging (LIDAR), optical coherence tomography (OCT), and high-resolution laser spectroscopy. The most important performance criteria are wavelength tuning ratio ($\Delta\lambda/\lambda_C$) and sweep speed. Vertical-cavity surface-emitting lasers (VCSELs) with tuning capability [1] have exhibited many desirable attributes including wafer-scale fabrication and testing, continuous and wide tuning, small footprint, and low power consumption. With a very short cavity (2-10 μm), the VCSEL's wavelength can be tuned by varying the optical thickness of some of the DBR layers or the optical cavity. This may be accomplished by varying the refractive index of some of the layers [2–4] or their physical thicknesses. The former approach has yet to experimentally result in a wide sweep range. Alternatively, using a microelectromechanical system (MEMS) to physically change the optical cavity length, a wide, continuous tuning range has been demonstrated [5]. Since the first MEMS-tunable VCSEL reported in 1995, many advances have been reported for center wavelengths (λ_C) of 850 nm, 980 nm, 1060 nm, 1310 nm, and 1550 nm [6–13]. Conventional MEMS-tunable VCSELs are designed with a high optical intensity concentrated in the semiconductor portion [5–7]. This configuration is referred to as semiconductor cavity dominant (SCD) design. The tuning ratio of a SCD design is limited to ~3.5% by the relatively small free spectral range (FSR).

To increase the tuning range, researchers have designed VCSELs with a $\lambda_C/4$-thick anti-reflection (AR) layer with $n_{AR} = \sqrt{n_S}$ where n_S is the index of the topmost semiconductor

#344397 https://doi.org/10.1364/OE.27.001798
Journal © 2019 Received 5 Nov 2018; revised 6 Dec 2018; accepted 10 Dec 2018; published 22 Jan 2019

layer. This configuration was referred to as the extended cavity (EC) design in [8]. In this case, the semiconductor and air cavities are perfectly matched. They resonate as one cavity, as if the semiconductor cavity "extends" into the air region. Previously, a very large static tuning range of 102 nm centered at 1550 nm ($\Delta\lambda/\lambda_C = 6.6\%$) was reported for an electrically-pumped EC VCSEL using electro-thermal tuning [9]. Limited by the thermal time constant, the tuning speed is shown to be relatively slow at 215 Hz with a smaller dynamic sweep range of 87 nm ($\Delta\lambda/\lambda_C = 5.6\%$). The EC design has also been implemented at a center wavelength of 1050 nm with a swept tuning range of 63.8 nm ($\Delta\lambda/\lambda_C = 6.1\%$) and a faster sweep rate of 240 kHz [10]. Both devices utilize dielectric distributed Bragg reflectors (DBR) with a high index contrast to minimize the effective length of the cavity, increasing the FSR at the cost of increased fabrication complexity due to additional deposition steps or multiple oxidation layers.

Recently, a third configuration called the air cavity dominant (ACD) design was reported, which forces the optical field to be confined more significantly in the air cavity at the center wavelength [11]. This design led to a record tuning ratio of 6.9% for an electrically-pumped VCSEL, while allowing more flexible choices of materials and thicknesses in the semiconductor-air coupling (SAC) region and the bottom DBR.

In this study, we reveal the origin of the increased tuning range of the ACD design and the impact of the design on threshold material gain. The swept operation of the device is demonstrated, exhibiting a swept tuning ratio of 6.5% at a sweep rate of 550 kHz. The high sweep rate is attributed to the lightweight high-contrast grating (HCG) used as the tunable mirror [14].

2. Underlying physics of tunable VCSELs

Figure 1 shows the schematic and the scanning electron microscopy (SEM) image of our 1060-nm ACD HCG tunable VCSEL. The device consists of a semiconductor portion, a top HCG mirror, and an air gap in between forming an air cavity. The semiconductor portion (starting from the top) includes a semiconductor-air coupling (SAC) region, two pairs of p-DBRs ($Al_{0.12}Ga_{0.88}As$ high-index layer first, followed by $Al_{0.9}Ga_{0.1}As$ low-index layer, $Al_{0.12}Ga_{0.88}As$ high-index layer, and $Al_{0.98}Ga_{0.02}As$ layer for oxidation), a $1\lambda_C$ cavity with five quantum wells in the center, followed by 38.5 pairs of n-DBRs, all grown on an n-doped GaAs substrate. One can identify two longitudinally coupled cavities: one centered at the active cavity with quantum wells and a second centered at the air gap between the HCG and the semiconductor. As described in [11], the SAC region dictates the difference between the three designs: SCD, EC and ACD.

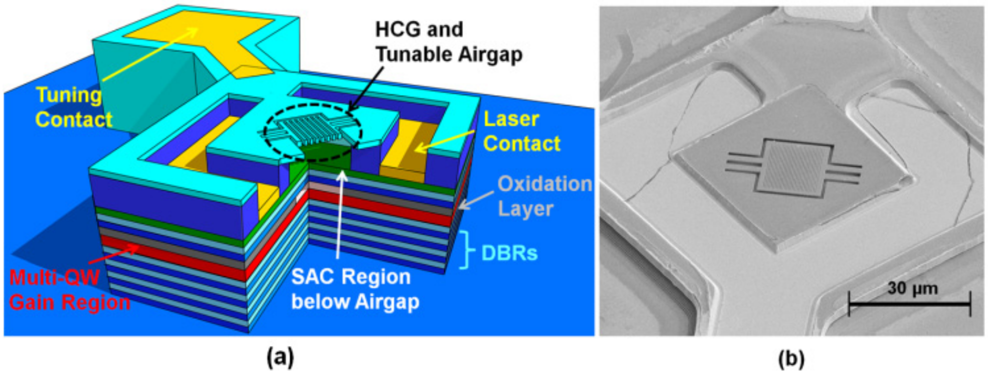

Fig. 1. (a) Schematic view of a MEMS-HCG tunable VCSEL with engineered semiconductor-air coupling (SAC) region. (b) Scanning electron microscope view of a fabricated 1060-nm MEMS-HCG tunable VCSEL.

To explore the underlying physics of the two cavities, we simplified the entire epitaxy stack to a $4\lambda_C$ semiconductor cavity with index n_S, a $\lambda_C/4$ SAC layer, and an air region of variable length (index 1), shown in Fig. 2(a).The semiconductor cavity was chosen to be $4\lambda_C$ to have a similar FSR to a realistic design. The structure is bounded on both sides by ideal reflectors which have Fresnel coefficients $r_1 = r_3 = 0.999 + 0i$ for all wavelengths. This eliminates the nonlinearity and discontinuities in the phase of the HCG and DBR reflectors, which allows the resonance lines in Fig. 2 to extend beyond the bandwidth of the real reflectors. When the mirrors are replaced with practical structures, the wavelength range will be sampled by the bandwidth of the DBR and the phase spectra of the reflectors will distort the tuning curve near the edges of the tuning range.

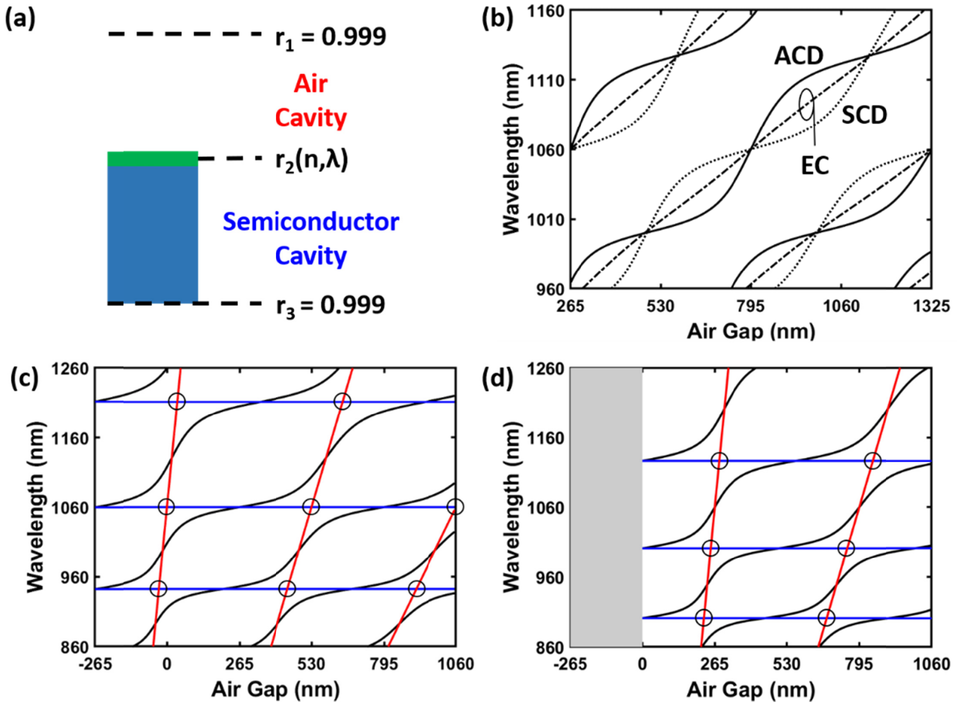

Fig. 2. Simplified coupled-cavity transfer-matrix analysis. (a) Illustration of simplified two coupled cavities with a semiconductor-air coupling (SAC) layer in-between. The $4\lambda_C$ semiconductor cavity with index n_S is shown in blue, the SAC layer with index n_{SAC} is shown in green, and the air cavity has an index of 1. The reflectors are indicated by dashed lines. (b) Comparison between SCD, EC, and ACD tuning characteristics with $n_{SAC} = 1$, n_{AR}, n_S respectively. The ACD design has the widest FSR when measured around the center wavelength of 1060 nm. (c) SCD and (d) ACD tuning curves plotted in black against semiconductor cavity modes in blue and air cavity modes in red. The circles indicate where the two families of lines cross, which results in anti-crossing in the (black) resonance lines of the full structures.

We consider three refractive index values for the $\lambda_C/4$ SAC layer, $n_{SAC} = 1$, n_{AR}, or n_S, representing SCD, EC, and ACD cases, respectively. The resonances of the simplified coupled-cavity structure for the three cases are calculated using the transfer matrix method by finding the wavelengths with zero round-trip phase for each air cavity length and are plotted as a function of air cavity length, as shown in Fig. 2(b), for all three cases. The EC case has Fabry-Perot (FP) wavelength linearly dependent on the air cavity length since the entire structure is one cavity. However, the SCD and ACD have distinctly different curvatures. This behavior is the same as shown in Fig. 13 of [11] with a full VCSEL design.

To understand the curvatures of the SCD and ACD resonance lines, we examine the two cavities: the air cavity defined by r_1 and r_2, and the semiconductor cavity defined by r_2 and r_3. The FP resonances for the semiconductor cavity, computed by removing r_1 from the transfer matrix simulation described above and plotted in blue in Figs. 2(c) and 2(d), are horizontal lines since they do not depend on the air cavity length. The FP resonances for the air cavity between r_1 and r_2, computed by removing r_3 from the simulation and plotted in red in Figs. 2(c) and 2(d), are linearly proportional to the air cavity length. Coupling between the semiconductor cavity and air cavity occurs when the two families of lines intersect each other, marked with circles on Figs. 2(c) and 2(d). The FP resonances of the full structure follows these two families of lines but avoid the crossings as shown by the black curved traces.

Figure 2(c) shows the case where $n_{SAC} = 1$. The semiconductor cavity is in resonance at $\lambda_C = 1060$ nm and thus a blue line is shown at the center wavelength 1060 nm. At an air gap of $-\lambda_C/4$, r_1 directly touches the semiconductor cavity. The full structure resonance lines are coincident with the semiconductor cavity resonance lines. As the air gap increases, an avoided crossing causes the full structure resonance to follow the air cavity resonance. Eventually, the full structure resonance avoids a second crossing to switch back to following the semiconductor resonance line. Since there is a semiconductor resonance at λ_C, the full structure resonance shows a low tuning slope at the center wavelength. This is the characteristic feature of an SCD design.

Figure 2(d) shows the case where $n_{SAC} = n_S$. Due to the $\lambda_C/4$ SAC refractive index, the FP wavelengths for the semiconductor cavity are shifted from those in the SCD case (Fig. 2(c)). In this ACD case, the semiconductor cavity is in *anti*resonance at λ_C, with the nearest FP modes located instead at 1130.7 and 997.6 nm. Again, the full structure resonance lines begin coincident with the semiconductor lines at an air cavity length of 0. The VCSEL resonance curves avoid the crossings between semiconductor and air resonances as air cavity length increases. Since the semiconductor cavity is in antiresonance at λ_C, the full structure resonance follows the air cavity resonance, resulting in a large tuning slope. This represents the ACD case. A stronger coupling between the semiconductor and air cavities in either an ACD or SCD design pushes the black lines apart, approaching the tuning characteristic for the EC case, in which the cavities are perfectly coupled.

The mathematical origin of the semiconductor resonances lies in the phase of r_2. If $n_{SAC} < n_{AR}$, then the interface between the semiconductor cavity and the SAC layer dominates r_2. The reflection phase into the semiconductor cavity, $\angle r_2(\lambda_C)$, is zero, and the semiconductor cavity is in resonance at λ_C. For the special case in which $n_{SAC} \cong n_{AR}$, the magnitude of r_2 is insignificant and the VCSEL cavity resonates as a unit. If $n_{SAC} > n_{AR}$, then the interface between the air cavity and the $\lambda_C/4$ SAC layer dominates r_2. The reflection phase $\angle r_2(\lambda_C) = \pi$, the semiconductor cavity is in antiresonance at λ_C, and the design is ACD. Note this description is very general and applies to more complex designs, such as that depicted in Fig. 1, which has two pairs of p-DBR between the $1\lambda_C$ cavity and the SAC, and the SAC consists of a window ($\lambda_C/2$) layer between the $\lambda_C/4$ n_{SAC} layer and air cavity.

For a typical tunable MEMS-VCSEL design, the air cavity length is chosen to be large enough to allow large tuning range with a maximum MEMS movement approximately 1/3 of the air gap. The FSR is thus the limiting factor in tunable VCSEL designs. As noted above, FSR is not constant with changing air cavity length. The range-limiting FSR is the shortest wavelength difference between the modes directly above and directly below the center wavelength, as these are the modes which are able to achieve threshold. In both ACD and SCD designs, the highest FSR is located near the intersections of the VCSEL cavity modes and the semiconductor cavity modes. Since the semiconductor cavity modes are off-center in an ACD VCSEL, the FSR is highest when the VCSEL resonance is far from the center of its tuning range. In contrast, the FSR of an SCD VCSEL is decreased as the VCSEL resonance moves away from the tuning center. The difference in FSR is illustrated in Fig. 2(b), which shows the VCSEL cavity modes for SCD, EC, and ACD designs. With this model, it is clear that to obtain a large tuning ratio, it is important to design an antiresonant semiconductor cavity with minimum length and reduce the coupling between the two cavities. In other words, it is best to let the air cavity dominate.

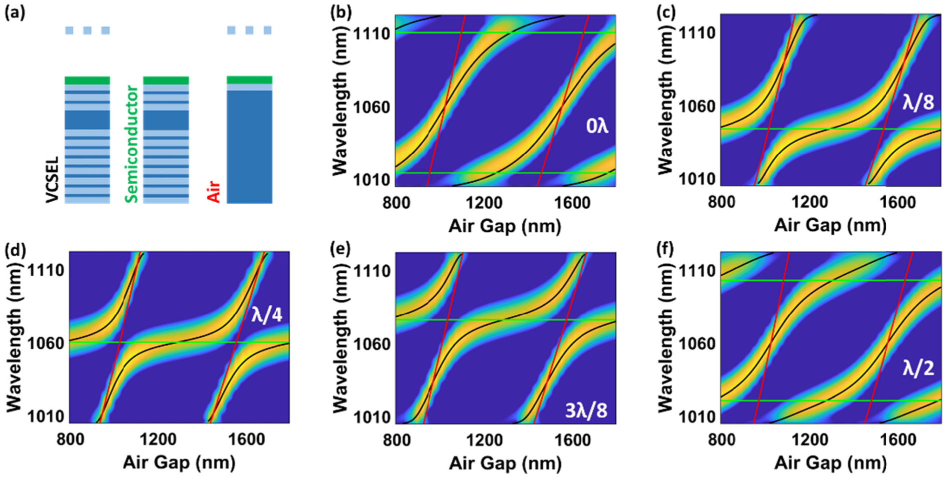

Fig. 3. FP Resonance as a function of air cavity thickness for a realistic VCSEL cavity using transfer-matrix and FDTD analysis. (a) Schematic of VCSEL structure, semiconductor cavity structure, and air cavity structure used to compute Fabry-Perot modes. The SAC region contains a high-index $\lambda_C/2$ "window" layer on top of a low-index $\lambda_C/4$ layer with n_{low}, both indices $>n_{AR}$. (b)-(f) Transfer matrix simulations for VCSEL modes (black), semiconductor cavity modes (green), and air cavity modes (red), inscribed on a resonance colormap from FDTD simulations of the full VCSEL structure. The thickness of the "window" layer is varied from 0 to $\lambda_C/2$, illustrating the shift from ACD at 0 to SCD at $\lambda_C/4$ and back to ACD at $\lambda_C/2$.

3. FDTD simulation of full structure

The above simplified model is next verified by FDTD simulation of a realistic VCSEL structure without active layers. Figure 3(a) shows the structure consisting of regions of $n_{high} = 3.483$ and $n_{low} = 2.988$, both $> n_{AR}$. From top to bottom, there is an HCG, a tunable air cavity, a SAC region, a 2-pair DBR, a $1\lambda_C$ high-index cavity, a 38.5-pair DBR, and a high-index substrate of infinite thickness. The SAC region contains a high-index $\lambda_C/2$ window layer on top of a low-index $\lambda_C/4$ layer with n_{low}. In this example, since there are limited choices of III-V epitaxy materials (refractive indices) for monolithic growth, we illustrate the coupling effect by changing the SAC window layer thickness instead by adding or removing a $\lambda_C/4$ layer.

In this structure, r_1 is the reflectivity of the HCG (computed using rigorous coupled-wave analysis [14]), r_2 is the reflectivity of the SAC region, and r_3 is the reflectivity of the 38.5-pair DBR terminating in the substrate. The FDTD simulation in Figs. 3(b)–3(e) shows resonance lines of the entire structure as functions of air cavity length when the window layer is varied from 0 to $\lambda_C/2$. The color code indicates the strength of the cavity resonance (yellow is high Q and blue is low). The resonance for the air cavity, semiconductor cavity and the entire structure using transfer-matrix simulations are also plotted in the same plots for comparison. Excellent agreement is obtained between the two approaches.

Since the dominant interface contributing to r_2 is the interface between the window layer and the air gap, the semiconductor cavity is much more sensitive to changes in window layer thickness than the air cavity. As the thickness of the window layer increases, so does the wavelength of each semiconductor resonance. Meanwhile, the position and slope of the air cavity resonances remains almost constant. Since the tuning behavior is dominated by the semiconductor cavity resonance, any increase in the overall thickness of the semiconductor cavity corresponds to a shift in the tuning characteristic. When the thickness of the window layer is 0, the SAC simply consists of a low-index $\lambda_C/4$ layer (but the low index is still greater than n_{AR}). Hence, the semiconductor cavity is antiresonant with two semiconductor resonances at ~1010 and 1110 nm, as shown in Fig. 3(b). This is the ACD case. When the window has a thickness of $\lambda_C/4$, the semiconductor cavity is in resonance, resulting in an SCD tuning characteristic as shown in Fig. 3(d). With the window layer increased to $\lambda_C/2$, the device is again ACD, as shown in Fig. 3(f).

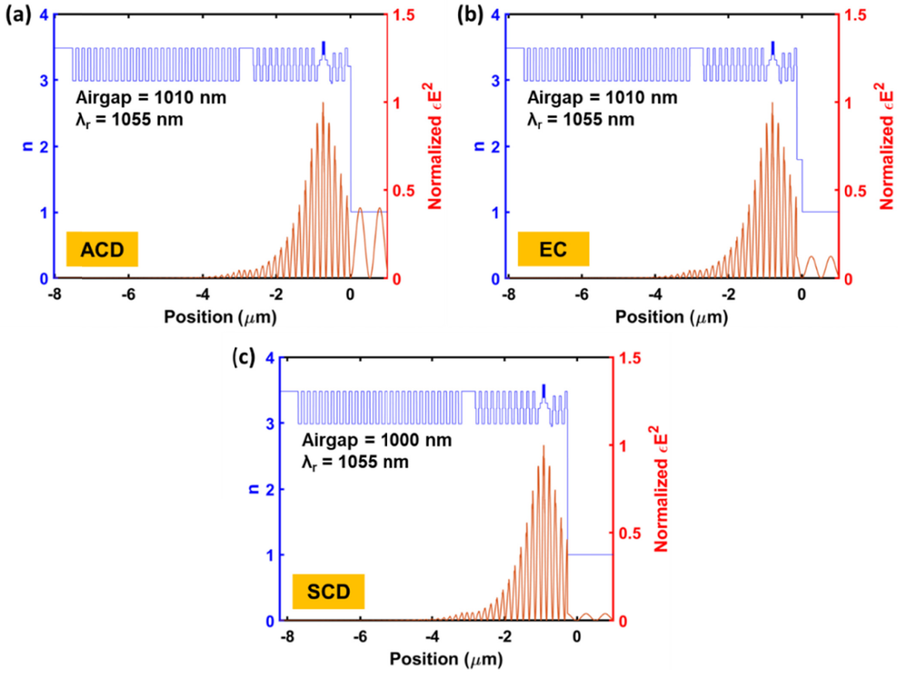

Fig. 4. Longitudinal electric energy density $\epsilon(z)|E(z)|^2$ profiles (red) calculated using the transfer-matrix method at tuning center where λ_r = 1060 nm for (a) ACD, (b) EC and (c) SCD. The refractive index (blue) for each layer is also plotted for each case to show the simulated structure.

4. Optical confinement

The optical confinement factor is an important parameter to examine since it determines the threshold current density. The real VCSEL structure, described in section one and shown in Fig. 1, is used for this study. The top $\lambda_C/4$ portion of semiconductor is InGaP in the real device (ACD) but is changed to Al_2O_3 in the EC design and air in the SCD device for comparison here. The longitudinal electric energy density $\epsilon(z)|E(z)|^2$ profiles at tuning center wavelength for ACD, EC, and SCD VCSELs are shown in Figs. 4(a), 4(b), and 4(c), respectively. At the tuning center, all three cases show the largest energy density inside the MQW region, which indicates a good field alignment. We indeed observe a relatively large energy distribution in the air cavity for ACD, in contrast to both EC and SCD. This confirms a strong coupling with the air cavity at the tuning center for the ACD case. Since ACD has more energy confined in the air sub-cavity, it should follow that the energy confinement factor for ACD is lower than EC and SCD.

To understand how the tuning impacts the laser threshold, we now calculate the effective cavity length observed from the semiconductor

$$L_{eff}(\lambda_r) = -\frac{\lambda_r^{2}}{4\pi n_g}\frac{\partial}{\partial\lambda}\left[\phi_{top}(\lambda)+\phi_{bottom}(\lambda)\right]_{\lambda=\lambda_r} \tag{1}$$

where $\phi_{top}(\lambda)$ and $\phi_{bottom}(\lambda)$ are reflective phases for the top and bottom mirrors seen by the semiconductor cavity [15]. In this approach, we consider the layers beneath the central quantum well as our bottom effective mirror and the layers above as the top effective mirror. Note that the effective length of the ACD design is the largest for all three designs at the tuning center.

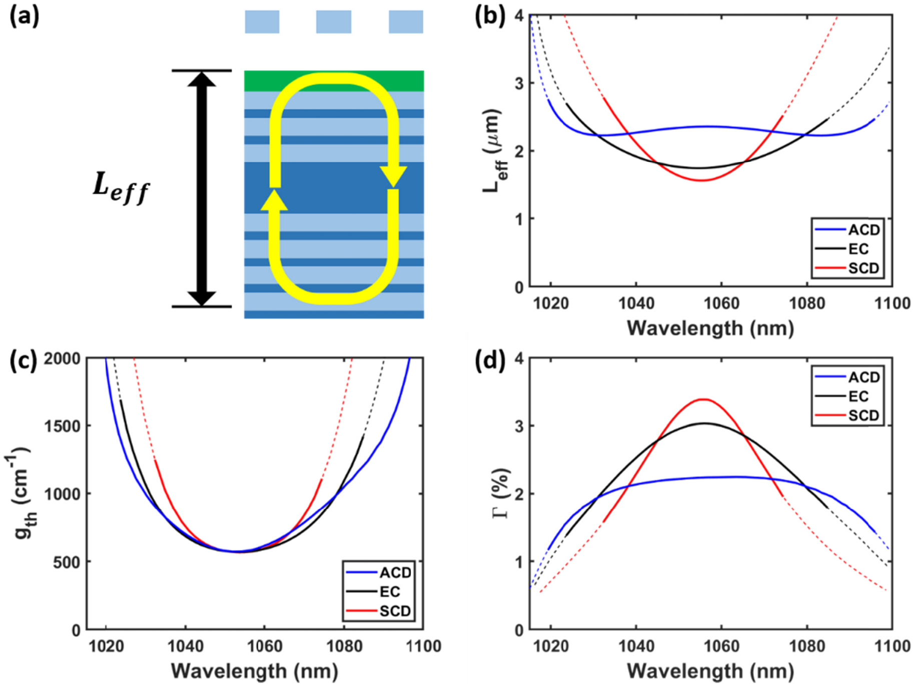

Fig. 5. Effective length is observed from the semiconductor cavity. (b) Total effective length L_{eff} as a function of resonance wavelength for SCD (red), EC (black), and ACD (blue) designs. (c) Threshold material gain g_{th} with uniform material loss α_i = 20 cm^{-1} added to all semiconductor layers. (d) Confinement factor calculated with $\Gamma = \alpha/g_{th}$.

However, the effective length for ACD stays relatively constant across the entire tuning range, whereas that of the SCD sharply increases as wavelength deviates from the center wavelength. Indeed, at the edges of the tuning range, the effective lengths of the SCD and EC devices become larger than that of the ACD device.

The threshold material gain is rigorously calculated as described in [11] for all three configurations and plotted in Fig. 5(c). Gain is added to the complex refractive index of the quantum well layers, and 20 cm^{-1} of loss is added to every other semiconductor layer. The transfer-matrix method is used to determine the round-trip gain of the cavity at the resonant wavelength. At threshold, the round-trip gain is equal to one. Since the internal loss is included in the calculation of the mirror reflectivity, the total loss in the cavity is given by

$$\Gamma g_{th} = \alpha = \frac{1}{2L_{eff}}\ln\left(\frac{1}{R_1 R_2}\right) \tag{2}$$

Rearranging Eq. (2) allows the calculation of the VCSEL's longitudinal confinement factor using the simulated threshold gain, effective length, and mirror reflectivities. The confinement factor is plotted as a function of resonant wavelength in Fig. 5(d). The ACD device has the lowest confinement factor of all three cases due to the large portion of electric energy confined in the air. Despite the significantly lower confinement factor of the ACD device, the threshold material gain at the tuning center is only increased by 1% because mirror loss and internal loss are both reduced at the center of the tuning range. Mirror loss is reduced in the ACD device by the higher L_{eff}, while internal loss is reduced by confining more energy in the lossless air gap.

The effective length and confinement factor calculations provide further insight into the threshold gain and FSR of the three designs. The FSR, which is inversely proportional to L_{eff}, is an important parameter at the tuning edge, where neighboring F-P modes may compete for the finite gain provided by the quantum wells. As shown in Fig. 5(b), the ACD design has the smallest effective length and thus the largest FSR at the tuning edge, confirming the trend noted in Fig. 2. The reduced effective length at the tuning edge in the ACD design also results in a higher confinement factor and lower threshold gain. As a result, using this novel ACD design, the threshold gain is not compromised significantly while the tuning range is largely extended.

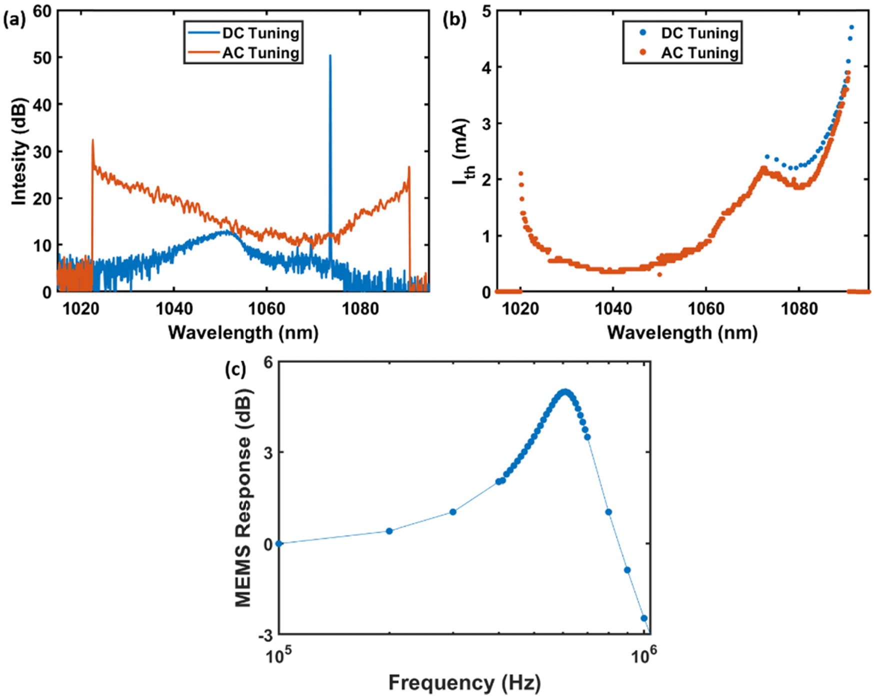

Fig. 6. (a) Measured swept VCSEL spectra for an ACD tunable VCSEL at 4.5 mA current injection under a constant DC bias (blue) and with an additional 550 kHz AC (red) tuning voltage. The swept spectrum covers a range of 68.38 nm, measured at −20 dB from the tuning edge peaks. (b) Threshold current measured with two different techniques. The curve in blue is measured by applying a series of DC tuning biases and measuring the threshold and wavelength at $1.1I_{th}$. The curve in red is measured by applying a DC tuning bias and sweeping the position of the HCG by applying a resonant AC signal, then measuring the emission spectrum at a series of laser drive currents. (c) The MEMS frequency response shows a resonance at 610 kHz and a −3-dB cutoff at 1.05 MHz.

5. Experimental results

The device shown in Fig. 1 is fabricated using process described in [11]. The GaAs sacrificial layer is removed by selective wet etching to form the 1.32 µm air gap. The SAC region of the actual device uses a design resembling the case shown in Fig. 3(f), with a $\lambda_C/2$ window layer composed of an InGaP etch stop and a GaAs contact layer on top of a $\lambda_C/4$ low-index layer.

Previously, with a combination of thermal, current and electrostatic tuning, single-mode continuous lasing across a 73-nm range was demonstrated [11]. With an optimized MEMS design, we obtain a continuous sweep by applying a DC tuning voltage of 31.5 V plus an AC tuning voltage of 10.0 V_{PP} at the mechanical resonance frequency of 550 kHz, as shown in Fig. 6(a). Resonant excitation of the mechanical structure displaces the mirror further than the equivalent DC voltage, eliminating the need for a tuning voltage high enough to break down the semiconductor junction [16]. The full dynamic tuning range is 68.38 nm, spanning from 1022.46 nm to 1090.84 nm, which is a direct proof of the extended FSR by our ACD design and is close to the calculated tuning range of 76 nm. If the AC voltage is increased to displace the MEMS further, the next Fabry-Perot mode will begin to lase over the same range of wavelengths. This shows that the tuning range is FSR limited and not threshold limited.

The threshold current for each wavelength is determined using the swept spectrum. The DC tuning bias, AC amplitude, and AC frequency are set such that the movement of the mirror traces one period of the tuning curve. A series of DC currents, ranging from 0.1 mA to 4 mA in steps of 0.05 mA, is applied through the laser diode. For each DC current, the emission spectrum is measured. The threshold at each wavelength is then determined by numerically differentiating the spectral intensity with respect to laser diode current and locating the abrupt step corresponding to the threshold. The results of this measurement are shown in Fig. 6(b). For comparison, the threshold current is also measured at a series of DC tuning biases.

The shape of the measured threshold current plotted versus wavelength in Fig. 6(b) deviates from the shape of the simulated threshold material gain curve in Fig. 5(c) in several aspects. First, the minimum threshold is blue-shifted to 1040 nm due to differences in HCG dimensions caused by variation in the lithography and etch processes. The second deviation is the peak at 1075 nm found in both the AC and DC measurements. This peak corresponds to a transition between two transverse modes. Transverse mode suppression is achieved in non-tunable oxide VCSELs by placing an oxide aperture near a longitudinal intensity node of the desired Fabry-Perot mode. In a tunable VCSEL, the position of the oxide layer with respect to the mode changes with wavelength, which can cause different transverse modes to dominate at different wavelengths. In the future, different transverse control mechanisms such as multiple oxide apertures, ion implantation, or buried heterostructure can be used to eliminate higher order transverse modes during tuning. Chirped QWs could also be used to reduce wavelength dependence in threshold current.

6. Conclusion

In summary, we investigate the mechanism behind the ACD configuration's large tuning range improvement over SCD and EC tunable VCSELs, finding that an antiresonance in the semiconductor cavity at the center wavelength is the cause for the high tuning slope and wide FSR. Our measurements of ACD devices confirm our theory of tuning ratio enhancement, demonstrating electrically pumped VCSELs with a high tuning ratio of 6.5% with resonant MEMS tuning at 550 kHz.

References

1. C. J. Chang-Hasnain, "Tunable VCSEL," IEEE J. Sel. Top. Quantum Electron. **6**(6), 978–987 (2000).
2. C. J. Chang-Hasnain, J. P. Harbison, C. E. Zah, L. T. Florez, and N. C. Andreadakis, "Continuous wavelength tuning of two-electrode vertical cavity surface emitting lasers," Electron. Lett. **27**(11), 1002–1003 (1991).

3. P. R. Berger, N. K. Dutta, K. D. Choquette, G. Hasnain, and N. Chand, "Monolithic Peltier-cooled vertical-cavity surface-emitting lasers," Appl. Phys. Lett. **59**(1), 117–119 (1991).
4. L. Frasunkiewicz, T. Czyszanowski, H. Thienpont, and K. Panajotov, "Electrically tunable VCSEL with intra-cavity liquid crystal: Design, optimization, and analysis of polarization- and mode-stability," Opt. Commun. **427**, 271–277 (2018).
5. M. S. Wu, E. C. Vail, G. S. Li, W. Yuen, and C. J. Chang-Hasnain, "Tunable micromachined vertical cavity surface emitting laser," Electron. Lett. **31**(19), 1671–1672 (1995).
6. M. C. Y. Huang, Y. Zhou, and C. J. Chang-Hasnain, "A nanoelectromechanical tunable laser," Nat. Photonics **2**(3), 180–184 (2008).
7. Y. Rao, W. Yang, C. Chase, M. C. Y. Huang, D. P. Worland, S. Khaleghi, M. R. Chitgarha, M. Zivadi, A. E. Willner, and C. J. Chang-Hasnain, "Long-wavelength VCSEL using high contrast grating," IEEE J. Sel. Top. Quantum Electron. **19**(4), 1701311 (2013).
8. F. Sugihwo, M. C. Larson, and J. S. Harris, Jr., "Micromachined widely tunable vertical cavity laser diodes," J. Microelectromech. Syst. **7**(1), 48–55 (1998).
9. C. Gierl, T. Gründl, K. Zogal, H. A. Davani, C. Grasse, G. Böhm, F. Küppers, P. Meissner, and M.-C. Amann, "Surface micromachined MEMS-tunable VCSELs with wide and fast wavelength tuning," Electron. Lett. **47**(22), 1243–1244 (2011).
10. D. D. John, C. B. Burgner, B. Potsaid, M. E. Robertson, B. K. Lee, W. J. Choi, A. E. Cable, J. G. Fujimoto, and V. Jayaraman, "Wideband electrically pumped 1050-nm MEMS-tunable VCSEL for opthalmic imaging," J. Lightwave Technol. **33**(16), 3461–3468 (2015).
11. P. Qiao, K. T. Cook, K. Li, and C. Chang-Hasnain, "Wavelength-Swept VCSELs," IEEE J. Sel. Top. Quantum Electron. **23**(6), 1700516 (2017).
12. E. Haglund, J. S. Gustavsson, J. Bengtsson, Å. Haglund, A. Larsson, D. Fattal, W. Sorin, and M. Tan, "Demonstration of post-growth wavelength setting of VCSELs using high-contrast gratings," Opt. Express **24**(3), 1999–2005 (2016).
13. I. S. Chung, V. Iakovlev, A. Sirbu, A. Mereuta, A. Caliman, E. Kapon, and J. Mork, "Broadband MEMS-tunable high-index-contrast subwavelength grating long-wavelength VCSEL," IEEE J. Quantum Electron. **46**(9), 1245–1253 (2010).
14. P. Qiao, W. Yang, and C. J. Chang-Hasnain, "Recent advances in high-contrast metastructures, metasurfaces, and photonic crystals," Adv. Opt. Photonics **10**(1), 180–245 (2018).
15. L. A. Coldren, S. W. Corzine, and M. L. Mašanović, *Diode Lasers and Photonic Integrated Circuits* (John Wiley & Sons, 2012).
16. T. Ansbaek, I. S. Chung, E. S. Semenova, O. Hansen, and K. Yvind, "Resonant MEMS tunable VCSEL," IEEE J. Sel. Top. Quantum Electron. **19**(4), 1702306 (2013).